# Dynamic Full-Field Imaging of Rupture Radiation: Material Contrast Governs Source Mechanism

J. Aichele, S. Latour, S. Catheline, P. Roux

Geophysical Research Letters

RESEARCH LETTER
10.1029/2022GL100473

**Key Points:**

- Noninvasive elastic near-field laboratory observations reveal source mechanisms of micro-slips, supershear and sub-Rayleigh ruptures
- Strong material contrasts as encountered in glacier stick-slip and landslides cause single force micro-slips and supershear ruptures
- Weak contrasts, which are found in natural faults, show a double-couple mechanism that is at times preceded by a slowly rising single force

**Supporting Information:**

Supporting Information may be found in the online version of this article.

**Correspondence to:**

J. Aichele,
johannes.aichele@rwth-aachen.de

**Citation:**

Aichele, J., Latour, S., Catheline, S., & Roux, P. (2023). Dynamic full-field imaging of rupture radiation: Material contrast governs source mechanism. *Geophysical Research Letters*, *50*, e2022GL100473. https://doi.org/10.1029/2022GL100473

Received 22 JUL 2022
Accepted 9 NOV 2022

**Author Contributions:**

**Conceptualization:** J. Aichele, S. Latour, S. Catheline, P. Roux
**Formal analysis:** J. Aichele, S. Latour, S. Catheline, P. Roux
**Funding acquisition:** S. Catheline, P. Roux
**Investigation:** J. Aichele
**Methodology:** J. Aichele, S. Latour, S. Catheline, P. Roux
**Project Administration:** S. Catheline, P. Roux
**Resources:** P. Roux
**Software:** J. Aichele
**Supervision:** S. Catheline, P. Roux
**Validation:** J. Aichele



# Dynamic Full-Field Imaging of Rupture Radiation: Material Contrast Governs Source Mechanism

**J. Aichele[1,2], S. Latour[3], S. Catheline[1], and P. Roux[2]**

[1]Laboratory of Therapeutic Applications of Ultrasound, INSERM & University of Lyon, Lyon, France, [2]ISTerre, University Grenoble Alpes, University Savoie Mont Blanc, CNRS, IRD, University Gustave Eiffel, Grenoble, France, [3]Institute of Astrophysics and Planetology, IRAP & University of Toulouse III, Toulouse, France

**Abstract** In seismology, the rupture mechanisms of an earthquake, a glacier stick-slip and a landslide are not directly observed, but inferred from surface measurements. In contrast, laboratory experiments can illuminate near field effects. The near field reflects the rupture mechanism but is highly attenuated in the case of real-world surface data. We directly image the elastic wave-field of a nucleating rupture non-invasively in its near-field with ultrasound speckle correlation. Our imaging yields the particle velocity of the full shear wave field at the source location and inside the 3D frictional body. We experimentally show that a strong bimaterial contrast, as encountered in environmental seismology, yields a unidirectional or linear force mechanism for pre-rupture microslips and decelerating supershear ruptures. A weak contrast, characteristic for earthquakes, generates a double-couple source mechanism for sub-Rayleigh ruptures, sometimes preceded by slow deformation at the interface. This deformation is reproduced by the NF of a unidirectional force.

**Plain Language Summary** Earthquakes, avalanches, icequakes and landslides originate from a common process: rupture at a material interface. During a rupture, for example, when a landslide slips, a characteristic pattern of seismic waves is created. This pattern differs at the earth's surface and the rupture interface, which is the source of the seismic waves inside the earth. Usually scientists only measure the waves arriving at the surface and need to deduce the wave pattern inside the earth from the surface measurement. We build a laboratory experiment which enables us to film wave propagation around the rupture surface, as if we had a camera inside the material. We film waves emitted during and prior to a rupture. For a soft material on a hard surface, such as encountered in icequakes or landslides, a single force model better explains the observed wave pattern than the commonly used model of four distributed forces. The rupture moves faster than shear waves propagate which results in a supershear cone, the elastic equivalent to the acoustic Mach cone created by supersonic aircrafts. For two materials of similar hardness, such as encountered in earthquakes, the classic model of four forces better explains the ruptures, which travel at sub-shear speed.

## 1. Introduction

For most earthquakes, the longstanding discussion on the appropriate representation of the earthquake source has been decided in favor of the double-couple (DC) source. It is the body force equivalent to slip on a fault and consists of two force couples acting at the earthquake source (Aki & Richards, 2009; Pujol, 2003). However, other rupture observations such as icequakes, landslides, induced seismicity and deep earthquakes are not always well reproduced by a standard DC model. For example, Ben-Zion and Ampuero (2009) theoretically show that brittle rupture is associated with a non-double-couple damage related source term. Kwiatek et al. (2011), Kwiatek and Ben-Zion (2013) discuss the presence of tensile opening during induced seismicity and aftershocks of a Mw 1.9 earthquake. In the case of glacial sliding, Ekström et al. (2003) report that a single force centroïd inversion outperforms standard moment tensor inversion (Harvard-CMT). In the laboratory, Lykotrafitis and Rosakis (2006) found indications for wrinkle-like rupture and tensile opening in a Homalite-on-steel friction experiment.

Inversion for earthquake sources is mostly done in the far-field and suffers from ambiguity. With the exception of volcanic seismicity, where hypocenters are shallow (Lokmer & Bean, 2010), the seismic near field (NF) suffers strong attenuation and is often concealed by ambient noise. In contrast to real-world seismic data, laboratory rupture experiments allow for dense instrumentation and direct imaging of rupture propagation. For example, the first unambiguous proof of supershear rupture was provided by strain imaging through photo-elastic experiments of sliding Homalite plates by Rosakis and Coker (1999). Recently, the group retrieved wave motion displacements

**Visualization:** J. Aichele, S. Latour
**Writing – original draft:** J. Aichele
**Writing – review & editing:** J. Aichele, S. Latour, S. Catheline, P. Roux

of supershear ruptures through digital image correlation (Rubino et al., 2020, 2022). Latour et al. (2011, 2013) introduced a new direct rupture imaging method using ultrafast ultrasound (US) that allows for observation of shear wave radiation during rupture propagation in soft materials: the shear wave's particle velocity is retrieved through speckle tracking of subsequent US backscatter images. In contrast to photo-elasticity, this method is not restricted to 2D setups. They show that during hydrogel-on-sandpaper friction the depinning of the gel is well matched by a singular bell shaped (Gaussian) shear point force. Furthermore, they observed the effects of barriers on rupture propagation on a hydrogel-glass interface with a granular inter-layer. At first glance hydrogels might seem counter-intuitive as earth material equivalents. However, they have been extensively used as geological analogs (van Otterloo & Cruden, 2016). An historic example is the jelly experiment of Reid (1910), that led to the elastic rebound theory. More recent examples include a subduction-analog gelatin setup (Corbi et al., 2011, 2017) and volcanic modeling (Kavanagh et al., 2018).

Here we investigate the source mechanism of the failure of a granular asperity in a laboratory friction experiment using a new setup based on the methodology introduced by Latour et al. (2011, 2013). Direct imaging of the NF of a propagating rupture allows us to compare the laboratory rupture to a kinematic rupture simulation using elastodynamic Green's functions. We compare a strong and a weak bimaterial contrast and test single-force and DC source models for different events to find the source mechanism depending on the elastic contrast and type of slip event.

## 2. Experimental Setup

All results are derived from the dynamic wave field imaging of two experimental scenarios: sliding of an asperity along an interface with a strong or a weak bimaterial contrast (Figure 1). The strong contrast is constituted of a glass - hydrogel (Polyvinyl-alcohol - PVA) interface (Figures 1a and 1b) and the weak contrast by a hydrogel-hydrogel interface (Figure 1d). For the strong contrast the shear wave speed ratio is several orders of magnitude: 7 m $s^{-1}$ (gel) versus >3,000 m $s^{-1}$ (glass) (Alexander et al., 2007; Dandekar, 1996). The hydrogels are homemade and non-standardized, and an elasticity contrast of the same order of magnitude remains for the weak contrast. The frictional behavior is ensured by a sand patch mimicking an asperity on a smooth surface. The glass plate is moved by a Kollmorgen stepper motor, which induces the deformation and subsequent sliding of the partly blocked gel via the frictional contact of the sand asperity. Seismic radiation is emitted upon failure of frictional contacts due to stick-slip ruptures, and is observed by ultrasonic speckle correlation imaging. The observation plane is centered in the gel, perpendicular to the interface and reaches from the asperity to the gel surface.

The imaging methodology is exemplary shown in Figure 1c for the weak interface experiment. Ultrasound backscatter images show a zone of high reflectivity at the gel-gel interface at 4 cm depth. It is caused by the sand layer in between the two hydrogels. Imaging below the interface is feasible, but the speckle quality is deteriorated due to strong US backscattering. In both gels, a 1 cm thick layer of intermediate reflectivity is observed next to the sand. It is likely caused by increased deposition of the backscatter agent (graphite). While graphite changes the ultrasonic impedance, shear wave propagation at the frequencies of interest remains unaffected. The phase correlation of successive US speckle images allows to resolve the shear wave induced vertical particle displacement between two snapshots, which is the apparent particle velocity $\frac{\partial u_z}{\partial t}$ (Pinton et al., 2005).

The dynamic observation is made possible by the high velocity contrast of the shear and compression waves in the hydrogel: while the compressional US travels at approximately 1,500 m $s^{-1}$, the rupture induced shear waves propagate at speeds below 10 m $s^{-1}$. Plane US pulses at high frame rate allow for the shear wave particle velocity to be temporally well resolved ($\Delta_t = 0.33$ ms). The US frequency (5 MHz) ensures the spatial resolution ($\lambda_{US} = 0.3$ mm). Hence, a shear wave propagating at 7 m $s^{-1}$ and 250 Hz is sampled at 25 US-wavelengths per shear wavelength ($\lambda_{shear} = 7$ mm). Consequently, the $z$-component of the entire transverse displacement field, including NF terms, is observed.

## 3. Kinematic Modeling of the Radiated Wavefield

The observed wavefield radiation is compared to kinematic wavefield modeling of equivalent body-force models (see Sections S2.6–S2.8 in Supporting Information S1), namely the single-force and douple-couple solutions. The source moves to simulate propagation of rupture fronts, and its velocity as well as the local source time functions are manually adjusted to obtain a good match to the data.

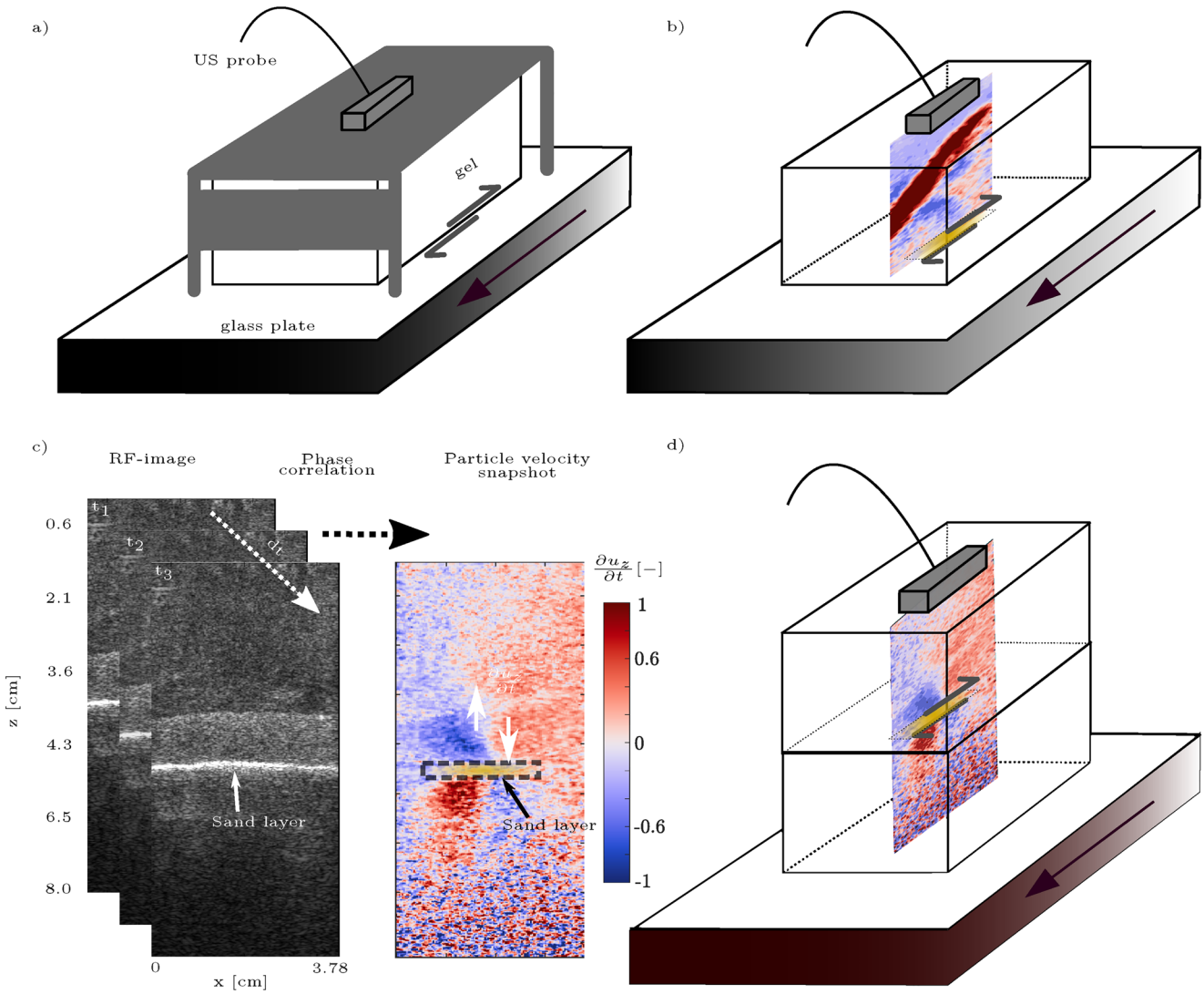


**Figure 1.** Experimental setup. (a) Schematic view of the montage. The gel is free at the interface and blocked above. (b) Imaging methodology: Correlation of successive ultrasound reflection images results in retrieval of the vertical component of the shear wave's particle velocity. Blue denotes upwards polarization (negative z) and red denotes downwards polarization. (b, d) Schematic illustration of the imaging plane in the bimaterial setups: (b) Strong bimaterial contrast: A hydrogel—sand asperity—glass interface (d) Weak bimaterial contrast: A hydrogel—sand asperity—hydrogel interface A detailed acquisition and processing workflow is given in Figure S1 in Supporting Information S1.

The displacement $u_{ij}(x, t)$ due to a unidirectional force (UF) in the $x_j$-direction with a source time function $X_0(t)$ at the source position is the convolution of $X_0$ with the elastodynamic impulse response (Green's function $G_{ij}$). It is the superposition of the compression and shear wave far-fields and the elastic NF:

$$\begin{aligned} u_i\left(\vec{x}, t\right) &= X_0 * G_{ij} \\ &= X_0 * {G_{ij}}^{Near} + X_0 * {G_{ij}}^{Far-P} + X_0 * {G_{ij}}^{Far-S} \end{aligned} \tag{1}$$

The full expression is given in Section S2.6 in Supporting Information S1 and a thorough derivation can be found in Aki and Richards (2009) Chapter 3–4.

In contrast to the UF-solution in Equation 1, the Green's function for a DC model can be separated into five physically meaningful terms: NF, intermediate S-field and P-field, and far S-field and P-field.

$$G_{DC} = G^{Near} + G^{IP} + G^{IS} + G^{FP} + G^{FS} \tag{2}$$

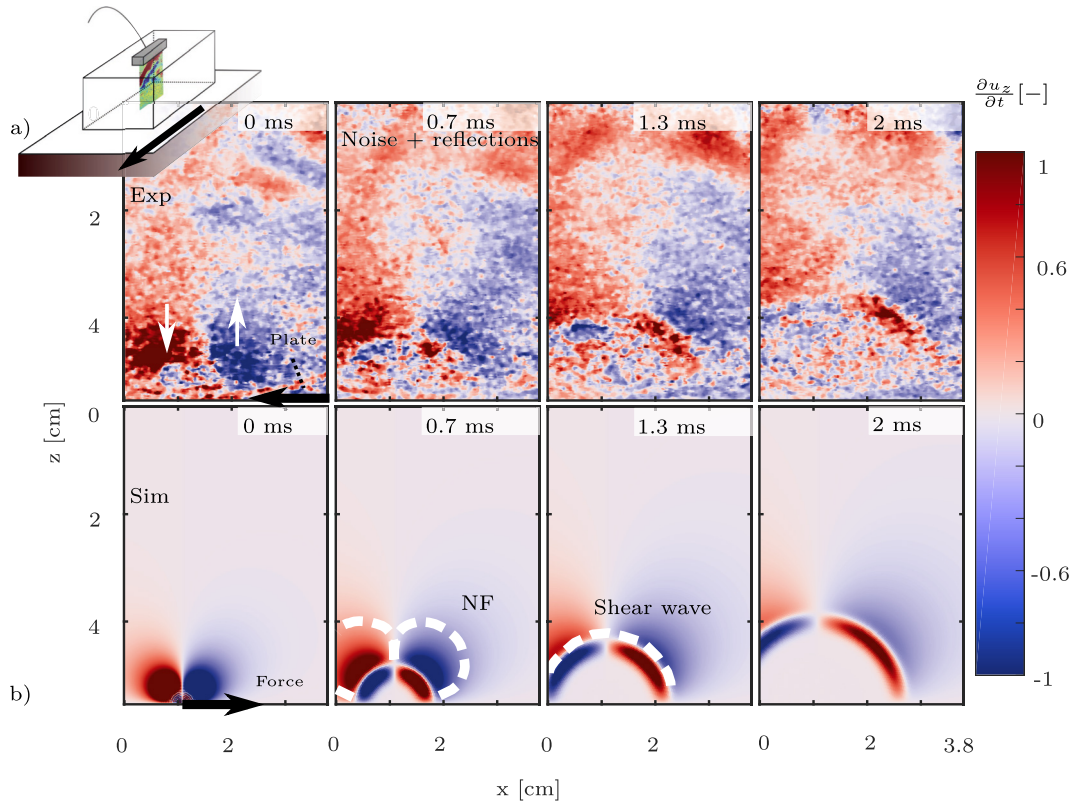


**Figure 2.** Strong material contrast: Comparison of an experimental micro-slip and simulation. Particle velocity polarization is indicated by the white arrows. (a) Particle velocities $\frac{\delta u_z}{\delta t}$ observed by shear wave imaging. The stepper motor drives the plate in negative x-direction. (b) Corresponding Green's function of a singular unidirectional shear force in positive x-direction. The near field lobe and shear wave front are indicated in panels (b).

The full analytical solution for the displacement field of a DC source can be found in Section S2.7 in Supporting Information S1.

In the following, we first present the results on the strong and weak contrast bimaterial interface and then discuss their relevance for natural rupture processes. Experiment and simulation are compared via wavefield snapshots that are normalized with respect to their time-series. The only filter applied is a spatial median filter.

## 4. Strong Bimaterial Contrast

The wavefield observations for the strong bimaterial contrast (Movie S1) reveals two types of slip events at the asperity: strongly localized micro-slips, and global stick-slip (see Figure S6 in Supporting Information S1) yielding propagating rupture fronts on asperity. We analyze one event of each type, representative of the overall observations.

For the microslip event, depicted in Figure 2a, a spherical wavefront is radiated from one location on the asperity. No rupture propagation is observed and consequently we model the event with a local point source in Figure 2b. The experimental radiation pattern is well reproduced by a unidirectional single force with a ramp shaped source time function $X_0(t)$. The first lobe represents the NF of the Green's function and is quickly attenuated. The second lobe is of opposite polarity and represents the far-field shear wave. The top 2 cm are artifacts of a previous event (see Figure S2 in Supporting Information S1 event 2–3). In contrast to the simulation, the experiment undergoes constant charging from the motor. Thus, noise as well as aseismic displacement due to deformation are present in the snapshots.

The Gaussian source time function employed by Latour et al. (2011) to model hydrogel-sandpaper depinning fails to reproduce the here observed wavefield. Our ramp shaped source time function with a rise time of 0.1 ms

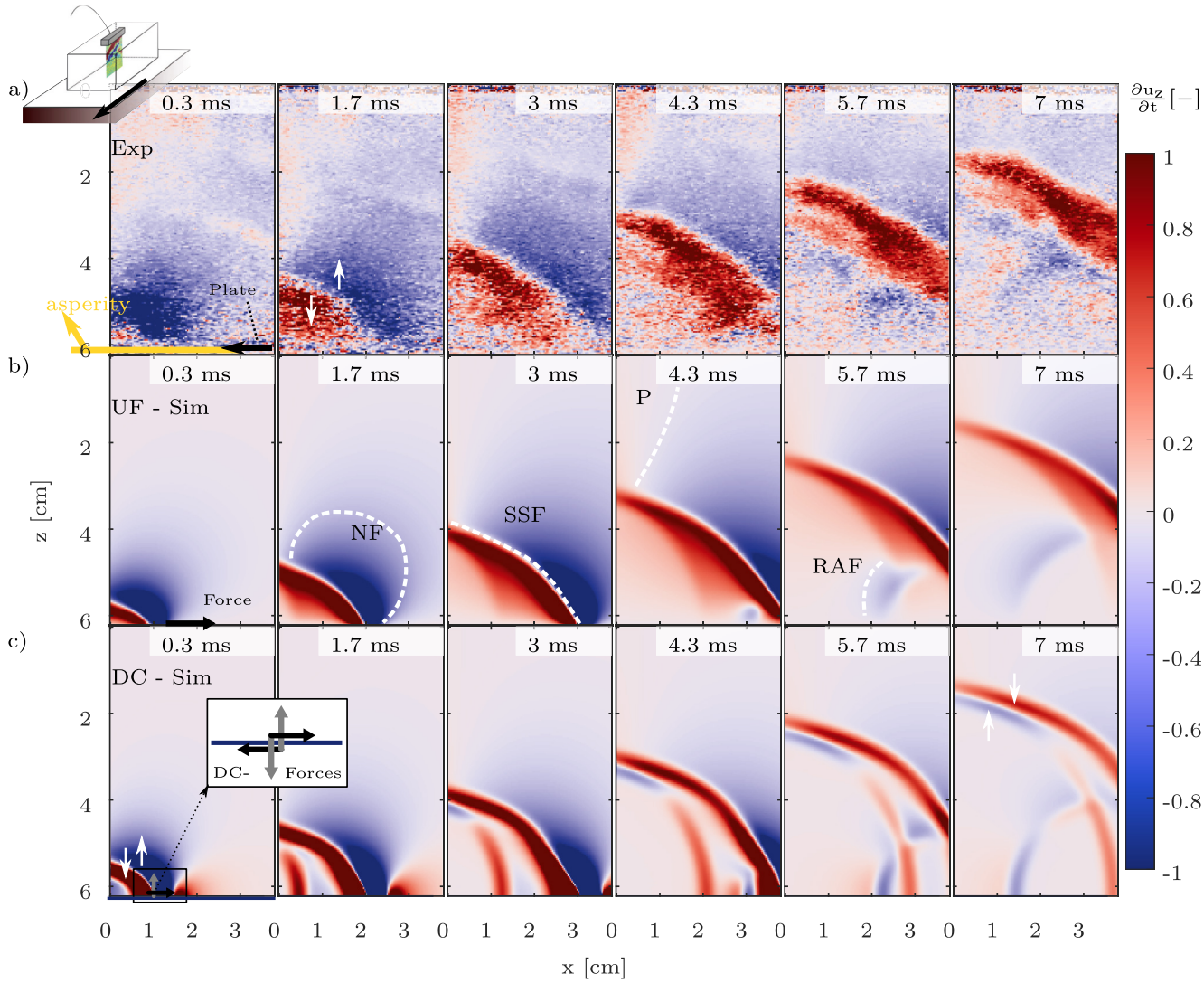


**Figure 3.** Strong material contrast: Comparison of an experimental supershear rupture and simulation. (a) $\frac{\delta u_z}{\delta t}$ as observed by shear wave imaging. The first snapshot is located 6 ms after the first snapshot of Figure 2. The motor drives the plate in negative x-direction. (b) $\frac{\delta u_z}{\delta t}$ resulting from the superposition of unidirectional shear forces in x-direction. Near field (NF), supershear front (SSF), P-wave imprint (P) and rupture arrest front (RAF) are indicated. (c) $\frac{\delta u_z}{\delta t}$ resulting from the superposition of double-couple point sources. The point sources in (b, c) point in positive x-direction and are shifted in time and space, in order to simulate a propagating rupture front (see Section S2.8 in Supporting Information S1). A higher time-resolution is given in Figures S4 and S5 in Supporting Information S1. The source functions and rupture speed profiles can be found in Figures S11 and S12 in Supporting Information S1.

(see Figure S10 in Supporting Information S1) results in a better match. A likely physical explanation is a localized change from a high- to low-stress state due to gel deformation and relaxation, which we model by a rightward pointing force (see Figure S10 in Supporting Information S1). Dynamically, this is equivalent to the plate displacement applying a left-pointing loading force to the gel, which drops to zero value. This localized shear friction drop on a micro-asperity might correspond to a highly localized inelastic dislocation or grain micro-slip in the granular layer.

The localized event of Figure 2 precedes a larger event, in which a rupture front traverses the entire visible interface (see Figure 3a; Figures S3 and S4 in Supporting Information S1 for details). The rupture propagation direction equals the sliding direction of the gel, that is, opposite to the plate movement. This observation agrees with Dedontney et al. (2011), who found that for bimaterial interfaces, ruptures will preferentially propagate in slip direction of the compliant side. The particle velocity $\left(\frac{\delta u_z}{\delta t}\right)$ measurements in Figure 3a are compared to two

analytic, kinematic simulations: a moving UF Figure 3b, and a moving DC Figure 3c. The simulations result from superposition of point sources along a decelerating speed profile, which is estimated roughly from the experimental data. Through trial and error we qualitatively match the NF lobe, supershear- and rupture arrest front (RAF). The source parameters are given in Figures S10–S14 in Supporting Information S1.

Key properties of the UF model, which are also present in the experimental observation, are indicated in Figure 3b. The first phase is an upwards polarized non-planar diffuse lobe. It corresponds to the NF of the right-traveling and rightwards pointing shear force. A sharp, downwards polarized large amplitude wave front follows, which is identified as a supershear front (SSF) in the simulation. It is the result of a rupture that breaks the asperity faster than the medium's shear wave speed. The front angle with the x-axis ($\beta = 21.8°$) at late observation times in Figure 3a and the measured shear wave speed ($c_s$) of $6.9 \pm 1$ m s$^{-1}$ (see Figure S15 in Supporting Information S1) are used to calculate an average rupture propagation speed ($c_r$) of $\approx$18 m s$^{-1}$: $c_r = \frac{c_s}{\sin(\beta)}$. However, two front angles can be identified throughout the rupture (see Figure S17 in Supporting Information S1). Furthermore, a time of flight measurement of the SSF along the rupture surface (see Figure S16 in Supporting Information S1) suggests a rupture speed above time resolution on 1 cm and below 12 m s$^{-1}$ afterward, indicating that the rupture is decelerating. Hence, we use a decreasing rupture velocity in the kinematic model. A low amplitude, downwards polarized wedge is present above the SSF. It corresponds to the imprint of the compressional (P) wave, which propagates at $\approx$1,500 m s$^{-1}$. Finally, a leftwards propagating and upwards polarized wavefront can be observed in the last snapshots of Figure 3a. In the simulations it is identified as the RAF, emitted at the asperity border.

In comparison, the best moving DC solution (Figure 3c) exhibits a high wavefield complexity which is absent in the experiment and the UF force simulation. Furthermore, the experimental data lack the leading, downwards polarized polarity of the DC simulation. However, at late times (7 ms), we can observe an upwards polarized front following the SSF, which has a counterpart in the DC solution (Figure 3c), but is absent in the UF simulation Figure 3b. To conclude, we find that the moving UF best matches the NF, the SSF and the RAF of the experimental data, but does not capture every detail of the wavefield. The remaining mismatch could stem from an oversimplified source-time function or an off-plane component due to a non-smooth surface. Such non-planar surfaces are encountered in real world ruptures as well.

## 5. Weak Bimaterial Contrast

The strong material contrast spanned three orders of magnitude. Now, the S-wave velocities are on the same order of magnitude: $6.9 \pm 1$ m s$^{-1}$ (lower gel) and $3.2 \pm 1$ m s$^{-1}$ (upper gel). However the effective speeds during the rupture might be different due to local heterogeneities and gel dehydration. We observe two types of slip events on the weak bimaterial contrast interface: propagating ruptures and localized wave radiations (see Movie S2).

A rupture that appears to propagate below shear and Rayleigh wave speed is shown in Figure 4a. Figures 4c and 4d show the corresponding 1D waveforms at specified depth- and time-steps in the upper halfspace. In both displays, the right-traveling front exhibits higher amplitudes than the left-traveling one. This front also exposes a smaller angle to the vertical (inclination difference), indicating a speed difference between the fronts. A straightforward explanation is a sub-Rayleigh rupture traveling in positive x-direction, the slip direction of the more compliant (upper) gel. A wavefront of continuous polarity throughout both half-spaces exists in the rupture propagation direction.

We model the radiation with a rightwards moving DC of constant sub-Rayleigh velocity (Figure S13 in Supporting Information S1). The simulated wavefield (Figures 4b, 4e, and 4f) reproduces the continuous polarity across the interface. In contrast, the radiation pattern of a UF exhibits alternating polarities (Figure S9 in Supporting Information S1). However, similar to the case of a strong bimaterial contrast, the leading NF lobe predicted by the DC solution is not identified in the experimental data. Figure 4a) reveals that a weak upwards polarized zone is present at interface depth, but quickly disappears elsewhere. This could be an imprint of the NF getting masked by the continuous deformation of the gel (see Movie S2, (Figures 4 and 5 start at approximately 2,396 ms),). Note that the amplitude increase in the rupture direction is more pronounced in the simulation than in the experiment. Shear wave attenuation could mask the amplitude difference between the wave fronts in rupture and opposite rupture direction, but is neglected in the kinematic simulation. Furthermore, the laboratory rupture might be shorter than the qualitatively simulated rupture of Figure 4b. For strong contrast experiments we as well as (Latour et al., 2011, 2013) only observed supershear ruptures. For homogeneous systems, rupture propagation at

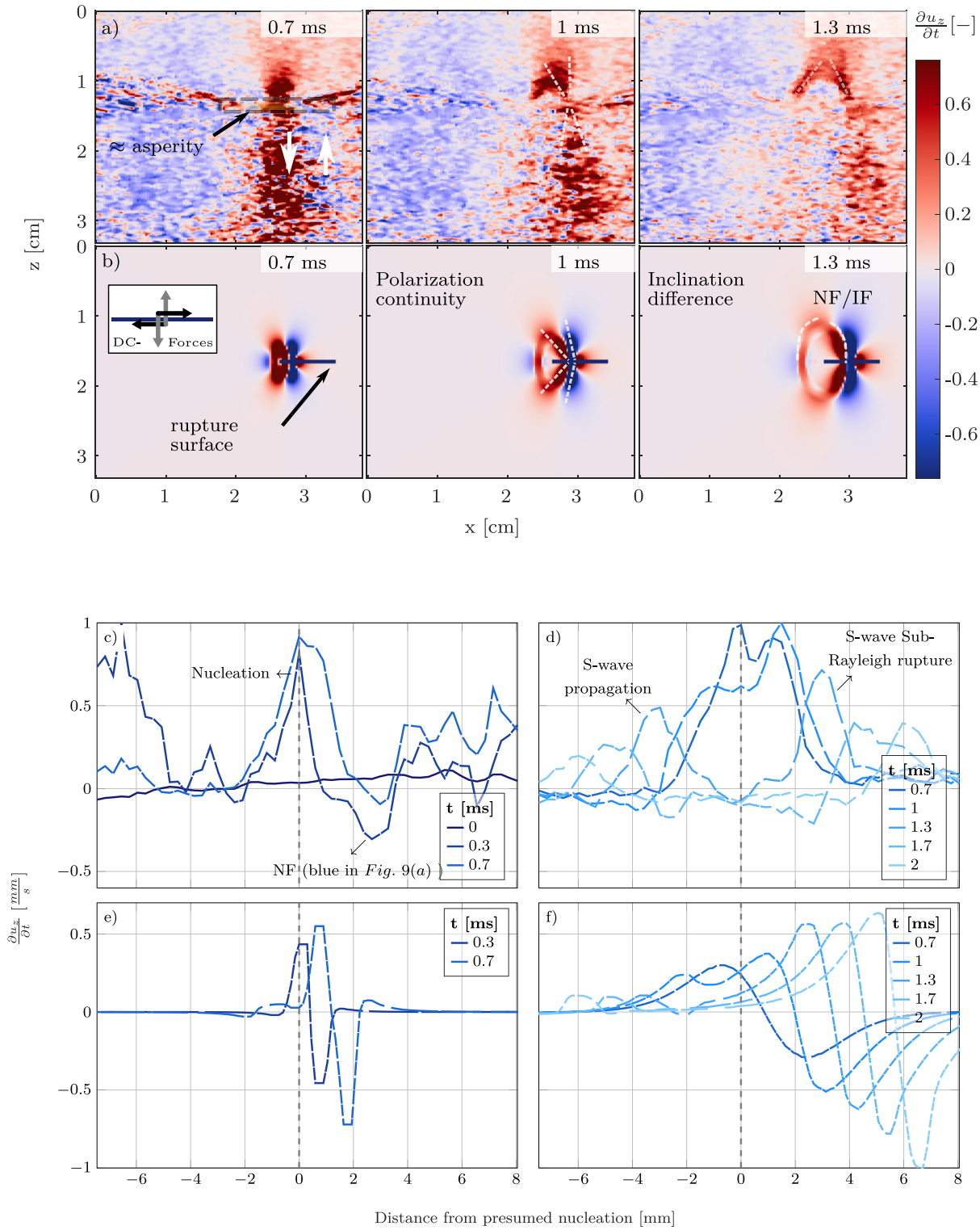


**Figure 4.** Weak material contrast: Comparison of sub-Rayleigh rupture observation and simulation. (a) Experimental particle velocities for a gel-gel rupture. (b) Right-traveling superposition of double-couple point sources at sub-Rayleigh speed with a ramp source function. NF, Near field, IF, Intermediate field. (c–f) Spatial Waveforms (x-direction) at fixed depth and time against distance to the presumed rupture nucleation point. (c) Experimental waveforms during rupture initiation (0–0.7 ms) at the gel-gel interface. The waveforms are a mean of 27 depthpoints (≈1 mm), just above the sand layer, which was identified from the ultrasound reflection images. The sand-layer to probe distance varies about 1.5 mm due to gel deformation and sand thickness. (d) Experimental waveforms of 0.7–2 ms ≈ 2 mm above the waveforms in (c). (e and f) Simulated waveforms corresponding to (c) and (d). Panel (e) is taken 0.2 mm and Panel (f) 3.8 mm above the simulated interface.

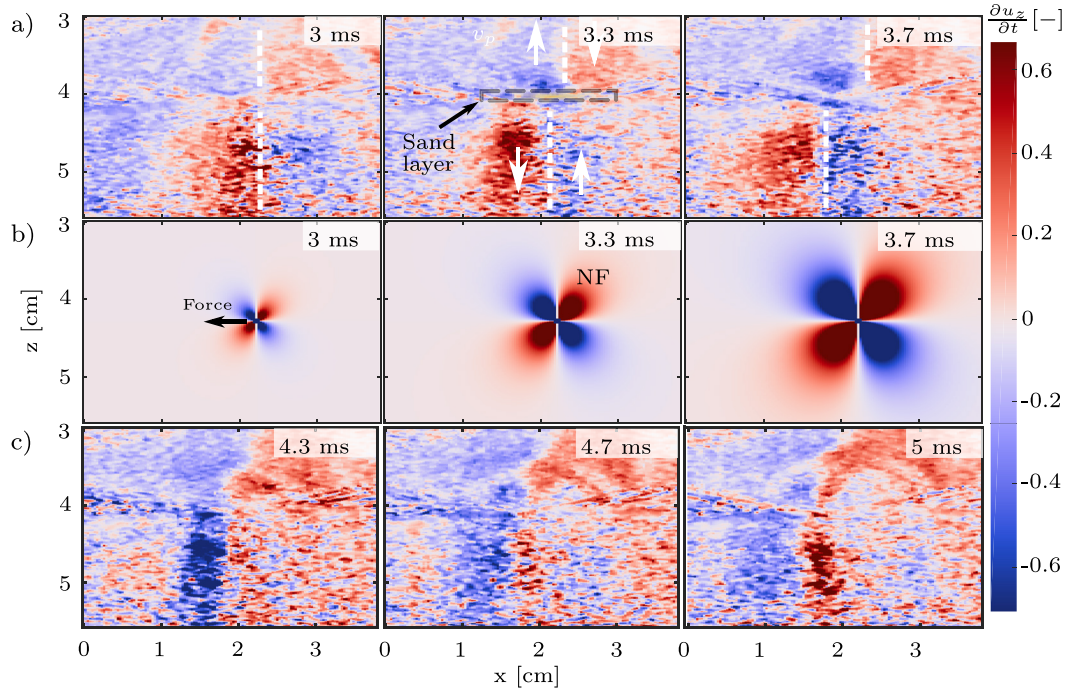


**Figure 5.** Weak bimaterial contrast: Comparison of a local event and a UF-simulation. (a) Experimental observation of an event 3 ms after the rupture of Figure 4. Decreased Signal-to-noise ratio below the indicated interface and the diagonal artifact at $t = 3$ ms are due to ultrasound diffraction at the sand. (b) Green's function simulation of a localized unidirectional shear force in negative x-direction using a 2.16 ms long rise time. NF, Near field. (c) Consequent time evolution of (a). The local event is followed or transforms into a rupture (see Movie S2 ≈2,400 ms).

sub-Rayleigh speed is expected (Shlomai & Fineberg, 2016), but had not been observed by shear wave imaging prior to this experiment, which provides the first dynamic US observation of a gel-gel rupture (Latour et al., 2011). However, we do not exclude the possibility that supershear ruptures may also exist in this case.

Situated 3 milliseconds after Figure 4 and 5a shows a localized event with a quadripolar radiation pattern. The radiation is qualitatively reproduced as the NF lobe of a unidirectional point force model, which is shown in Figure 5b. The source rise time is several ms long (see Figure S13 in Supporting Information S1). Contrary to the localized event on the strong bimaterial contrast interface, the far-field part of the theoretical radiation is not observed. Instead, the event is followed by a left-going rupture, shown in Figure 5c (event 3 in Figure S8 in Supporting Information S1). A similar sequence occurs at 2,350 ms in Movie S2. We hypothesize that the long rise-time localized event corresponds to the nucleation process of the subsequent rupture. An apparent aseismic lateral displacement of the radiation pattern in the lower half space for the experimental data remains of unclear origin.

## 6. Relevance for Natural Rupture Processes

For the strong bimaterial contrast, we find that microslip as well as rupture radiations are better described by a unique force model than by a DC model. This is intuitively understood as the consequence of the strong elasticity contrast at the interface: the UF corresponds to the relaxation of the gel's loading force when friction drops at the interface.

In nature, strong material contrasts are encountered in environmental seismology, that is, for landslides and glacier stick-slip. Both processes exhibit a wet granular layer and a compliant mass sliding on a hard bedrock. Our granular asperity is conceptually comparable to glacial till (Gräff et al., 2021), and the "sticky spot" encountered in alpine glacial stick-slip (Umlauft et al., 2021). Unidirectional force models for strong material contrasts have been proposed for the 1980 Mt. St. Helens eruption (Kanamori & Given, 1982) and the 1975 Kalapana, Hawaii, earthquake, where a large landslide occurred on Kilauea volcano (Eissler & Kanamori, 1987). In a theoretical

analysis Dahlen (1993) showed that brecciation in the sliding block of shallow landslides results in mechanical decoupling of the two fault sides. The decoupling leads to a single-force rupture source, pointing in the direction of the mass movement for decelerating sliding (Julian et al., 1998). Dahlen (1993) calculated that the shear wave speed of the landslide tends toward zero and must have been below 300 m $s^{-1}$, compared to 3,500 m $s^{-1}$ in the bedrock.

Ekström et al. (2003) found that for glacier stick-slip in Greenland, single force inversions perform better than standard moment tensor inversions. Again, this could be explained by the lower shear wave speed in ice. Lastly, Trottet et al. (2022) very recently showed rupture propagation at supershear speed for snow avalanches, another case exposing low shear wave speeds of the sliding mass (<120 m $s^{-1}$) and high material contrasts (0.5–2 vs. 5–30 MPa Young's modulus). Our direct experimental observation of the wavefield generation confirms, that unique force mechanisms are relevant for describing slip events between materials with strong wave velocity contrasts.

In global seismology, the earthquake source corresponds to slip on a planar fault and is widely modeled by a DC equivalent body source. Our closest analog experiment is the propagating rupture on the asperity at the gel-gel interface. We observe radiations best described by a moving DC, which indicates a coupling between both sides of the fault. However, some ruptures are preceded by localized events, which are reproduced by the NF radiation of a slowly rising UF. We hypothesize that one gel deforms preferentially during loading, as previously observed in rubber by Brune et al. (1993). It then slowly initiates relaxation as a preparatory process before both gels release the remaining deformation during rupture propagation. This non-symmetric process could be expedited by the sand layer that can locally decouple both sides of the fault through grain rearrangements. The single force source mechanism may be relevant for slow processes on natural faults. For example, shallow thrust faults expose an asymmetry in the fault loading, and fault gouge, damaged layers and fluids can constitute decoupling mechanisms.

## 7. Outlook

In the future the utilization of several imaging probes could allow the simultaneous measurement of fault-parallel and fault-orthogonal particle velocity (Aichele, 2019). The dense spatial sampling achieved through phase correlation would then allow for the local recovery of displacement and strain in 3D observations of the rupture-borne in situ elastic wavefield of complex asperities (Aichele, 2019).

## Data Availability Statement

The experimental data sets are available in Aichele (2022, https://zenodo.org/record/6886498) as *.mat and can be read with Matlab or scipy (python). The code to reproduce the simulations is available under Aichele (2022, https://zenodo.org/record/6886498) and JoTrab (2022, https://zenodo.org/record/7092715). Codes are confirmed to run under MATLAB (2020).

**Acknowledgments**
We are grateful to Christophe Voisin for discussions on rupture nucleation and Max Solazzo for finishing the friction bench. Many thanks also to the three anonymous reviewers for their excellent comments which greatly improved the present paper. The project has received funding from the European Union's Horizon 2020 research and innovation programme under the Marie Sklodowska-Curie Grant agreement No. 641943 (ITN WAVES) and resulted in the PHD thesis Aichele (2019). ISterre is part of Labex OSUG@2020.

## References

Aichele, J. (2019). *Elastic waves in complex conditions: From the onset of rupture to viscous dispersion in foams* (Doctoral dissertation, Université de Lyon). Retrieved from https://tel.archives-ouvertes.fr/tel-02481746

Aichele, J. (2022). *Dynamic full-field imaging of rupture radiation: Material contrast governs source mechanism*. Zenodo. Retrieved from https://zenodo.org/record/6886498

Aki, K., & Richards, P. G. (2009). Quantitative seismology. In *Book* (2nd ed., p. 700), University Science Books.

Alexander, C. S., Chhabildas, L. C., & Templeton, D. W. (2007). The Hugoniot elastic limit of soda-lime glass. In *AIP conference proceedings* (Vol. *955*, pp. 733–738). https://doi.org/10.1063/1.2833222

Ben-Zion, Y., & Ampuero, J.-P. (2009). Seismic radiation from regions sustaining material damage. *Geophysical Journal International*, *178*(3), 1351–1356. https://doi.org/10.1111/j.1365-246x.2009.04285.x

Brune, J. N., Brown, S., & Johnson, P. A. (1993). Rupture mechanism and interface separation in foam rubber models of earthquakes: A possible solution to the heat flow paradox and the paradox of large overthrusts. *Tectonophysics*, *218*(1–3), 59–67. https://doi.org/10.1016/0040-1951(93)90259-m

Corbi, F., Funiciello, F., Brizzi, S., Lallemand, S., & Rosenau, M. (2017). Control of asperities size and spacing on seismic behavior of subduction megathrusts. *Geophysical Research Letters*, *44*(16), 8227–8235. https://doi.org/10.1002/2017GL074182

Corbi, F., Funiciello, F., Faccenna, C., Ranalli, G., & Heuret, A. (2011). Seismic variability of subduction thrust faults: Insights from laboratory models. *Journal of Geophysical Research*, *116*(B6), B06304. https://doi.org/10.1029/2010jb007993

Dahlen, F. A. (1993). Single-force representation of shallow landslide sources. *Bulletin of the Seismological Society of America*, *83*(1), 130–143. https://doi.org/10.1785/BSSA0830010130

Dandekar, D. P. (1996). Optical and mechanical properties of soda lime glass under shock compression and release. In *International conference on structures under shock and impact, SUSI* (Vol. *22*, pp. 439–448).
Dedontney, N., Templeton-Barrett, E. L., Rice, J. R., & Dmowska, R. (2011). Influence of plastic deformation on bimaterial fault rupture directivity. *Journal of Geophysical Research*, *116*(10), B10312. https://doi.org/10.1029/2011JB008417
Eissler, H. K., & Kanamori, H. (1987). A single-force model for the 1975 Kalapana, Hawaii, Earthquake. *Journal of Geophysical Research*, *92*(B6), 4827–4836. https://doi.org/10.1029/JB092iB06p04827
Ekström, G., Nettles, M., & Abers, G. A. (2003). Glacial earthquakes. *Science*, *302*(5645), 1088057–1088624. https://doi.org/10.1126/science.1088057
Gräff, D., Köpfli, M., Lipovsky, B. P., Selvadurai, P. A., Farinotti, D., & Walter, F. (2021). Fine structure of microseismic glacial stick-slip. *Geophysical Research Letters*, *48*(22), e2021GL096043. https://doi.org/10.1029/2021gl096043
JoTrab. (2022). JoTrab/analytic_rupture_radiation: Release Review round 1 (v). *Zenodo*. https://doi.org/10.5281/zenodo.7092715
Julian, B. R., Miller, A. D., & Foulger, G. R. (1998). Non-double-couple earthquakes 1. Theory. *Reviews of Geophysics*, *36*(4), 525–549. https://doi.org/10.1029/98rg00716
Kanamori, H., & Given, J. W. (1982). Analysis of long-period seismic waves excited by the May 18, 1980, eruption of Mount St. Helens—A terrestrial monopole? *Journal of Geophysical Research*, *87*(B7), 5422–5432. https://doi.org/10.1029/jb087ib07p05422
Kavanagh, J. L., Engwell, S. L., & Martin, S. A. (2018). A review of laboratory and numerical modelling in volcanology. *Solid Earth*, *9*(2), 531–571. https://doi.org/10.5194/se-9-531-2018
Kwiatek, G., & Ben-Zion, Y. (2013). Assessment of P and S wave energy radiated from very small shear-tensile seismic events in a Deep South African mine. *Journal of Geophysical Research: Solid Earth*, *118*(7), 3630–3641. https://doi.org/10.1002/jgrb.50274
Kwiatek, G., Plenkers, K., Dresen, G., & JAGUARS Research Group. (2011). Source parameters of picoseismicity recorded at Mponeng deep gold mine, South Africa: Implications for scaling relations. *Bulletin of the Seismological Society of America*, *101*(6), 2592–2608. https://doi.org/10.1785/0120110094
Latour, S., Gallot, T., Catheline, S., Voisin, C., Renard, F., Larose, E., & Campillo, M. (2011). Ultrafast ultrasonic imaging of dynamic sliding friction in soft solids: The slow slip and the super-shear regimes. *EPL (Europhysics Letters)*, *96*, 59003. https://doi.org/10.1209/0295-5075/96/59003
Latour, S., Voisin, C., Renard, F., Larose, E., Catheline, S., & Campillo, M. (2013). Effect of fault heterogeneity on rupture dynamics: An experimental approach using ultrafast ultrasonic imaging. *Journal of Geophysical Research: Solid Earth*, *118*(11), 5888–5902. https://doi.org/10.1002/2013jb010231
Lokmer, I., & Bean, C. J. (2010). Properties of the near-field term and its effect on polarisation analysis and source locations of long-period (LP) and very-long-period (VLP) seismic events at volcanoes. *Journal of Volcanology and Geothermal Research*, *192*(1–2), 35–47. https://doi.org/10.1016/j.jvolgeores.2010.02.008
Lykotrafitis, G., & Rosakis, A. J. (2006). Dynamic sliding of frictionally held bimaterial interfaces subjected to impact shear loading. *Proceedings of the Royal Society A: Mathematical, Physical & Engineering Sciences*, *462*(2074), 2997–3026. https://doi.org/10.1098/rspa.2006.1703
MATLAB. (2020). *9.9.0.1718557 (R2020b)*. The MathWorks Inc.
Pinton, G., Dahl, J., & Trahey, G. (2005). Rapid tracking of small displacements with ultrasound. In *IEEE ultrasonics symposium* (Vol. 4, pp. 2062–2065). IEEE.
Pujol, J. (2003). The body force equivalent to an earthquake: A tutorial. *Seismological Research Letters*, *74*(2), 163–168. https://doi.org/10.1785/gssrl.74.2.163
Reid, H. (1910). The California earthquake of April 18, 1906, report of the state earthquake investigation commission, the mechanism of the earthquake. *Nature*, *2*(2128), 165–166. https://doi.org/10.1038/084165a0
Rosakis, A. J., & Coker, D. (1999). Cracks faster than the shear wave speed. *Science*, *284*, 1337–1340. https://doi.org/10.1126/science.284.5418.1337
Rubino, V., Lapusta, N., & Rosakis, A. J. (2022). Intermittent lab earthquakes in dynamically weakening fault gouge. *Nature*, *1–8*(7916), 922–929. https://doi.org/10.1038/s41586-022-04749-3
Rubino, V., Rosakis, A. J., & Lapusta, N. (2020). Spatiotemporal properties of sub-Rayleigh and supershear ruptures inferred from full-field dynamic imaging of laboratory experiments. *Journal of Geophysical Research: Solid Earth*, *125*(2), 1–25. https://doi.org/10.1029/2019JB018922
Shlomai, H., & Fineberg, J. (2016). The structure of slip-pulses and supershear ruptures driving slip in bimaterial friction. *Nature Communications*, *7*, 1–7. https://doi.org/10.1038/ncomms11787
Trottet, B., Simenhois, R., Bobillier, G., Bergfeld, B., van Herwijnen, A., Jiang, C., & Gaume, J. (2022). Transition from sub-Rayleigh anticrack to supershear crack propagation in snow avalanches. *Nature Physics*, *1–5*(9), 1094–1098. https://doi.org/10.1038/s41567-022-01662-4
Umlauft, J., Lindner, F., Roux, P., Mikesell, T. D., Haney, M. M., Korn, M., & Walter, F. T. (2021). Stick-slip tremor beneath an alpine glacier. *Geophysical Research Letters*, *48*(2), e2020GL090528. https://doi.org/10.1029/2020gl090528
van Otterloo, J., & Cruden, A. R. (2016). Rheology of pig skin gelatine: Defining the elastic domain and its thermal and mechanical properties for geological analogue experiment applications. *Tectonophysics*, *683*, 86–97. https://doi.org/10.1016/j.tecto.2016.06.019

## References From the Supporting Information

Andrews, D. J., & Ben-Zion, Y. (1997). Wrinkle-like slip pulse on a fault between different materials. *Journal of Geophysical Research*, *102*(B1), 553–571. https://doi.org/10.1029/96JB02856
Sandrin, L., Catheline, S., Tanter, M., Hennequin, X., & Fink, M. (1999). Time-resolved pulsed elastography with ultrafast ultrasonic imaging. *Ultrasonic Imaging*, *21*(4), 259–272. https://doi.org/10.1177/016173469902100402